

Simultaneous spatial and temporal focusing for axial scanning

Michael E. Durst, Guanghao Zhu, and Chris Xu

School of Applied and Engineering Physics, Cornell University, Ithaca, NY 14853
med43@cornell.edu

Abstract: We show theoretically and experimentally that simultaneous spatial and temporal focusing can scan the temporal focal plane axially by adjusting the group velocity dispersion in the excitation beam path. When the group velocity dispersion is small, the pulse width at the temporal focal plane is transform-limited, and the amount of shift depends linearly upon the dispersion. By adding a meter of large mode area fiber into the system, we demonstrate this axial scanning capability in a fiber delivery configuration. Because a transform-limited pulse width is automatically recovered at the temporal focal plane, simultaneous spatial and temporal focusing negates the need for any dispersion pre-compensation, further facilitating its integration into a fiber delivery system. A highly promising application for simultaneous spatial and temporal focusing is an axial scanning multiphoton fluorescence fiber probe without any moving parts at the distal end and without dispersion pre-compensation.

©2006 Optical Society of America

OCIS codes: (170.3880) Medical optics and biotechnology : Medical and biological imaging; (180.5810) Scanning microscopy

References and links

1. W. Denk, J. H. Strickler, and W. W. Webb, "2-Photon Laser Scanning Fluorescence Microscopy," *Science* **248**, 73-76 (1990).
2. J. C. Jung, and M. J. Schnitzer, "Multiphoton endoscopy," *Opt. Lett.* **28**, 902-904 (2003).
3. C. Liang, M. R. Descour, K. B. Sung, and R. Richards-Kortum, "Fiber confocal reflectance microscope (FCRM) for in-vivo imaging," *Opt. Express* **9**, 821-830 (2001).
4. K. B. Sung, C. N. Liang, M. Descour, T. Collier, M. Follen, and R. Richards-Kortum, "Fiber-optic confocal reflectance microscope with miniature objective for in vivo imaging of human tissues," *IEEE Trans. Biomed. Eng.* **49**, 1168-1172 (2002).
5. A. R. Rouse, A. Kano, J. A. Udovich, S. M. Kroto, and A. F. Gmitro, "Design and demonstration of a miniature catheter for a confocal microendoscope," *Appl. Opt.* **43**, 5763-5771 (2004).
6. W. Gobel, J. N. D. Kerr, A. Nimmerjahn, and F. Helmchen, "Miniaturized two-photon microscope based on a flexible coherent fiber bundle and a gradient-index lens objective," *Opt. Lett.* **29**, 2521-2523 (2004).
7. D. L. Dickensheets, and G. S. Kino, "Micromachined scanning confocal optical microscope," *Opt. Lett.* **21**, 764-766 (1996).
8. U. Hofmann, S. Muehlmann, M. Witt, K. Dorschel, R. Schutz, and B. Wagner, "Electrostatically driven micromirrors for a miniaturized confocal laser scanning microscope," *Proceedings of SPIE* **3878**, 29-38 (1999).
9. D. Bird, and M. Gu, "Two-photon fluorescence endoscopy with a micro-optic scanning head," *Opt. Lett.* **28**, 1552-1554 (2003).
10. F. Helmchen, M. S. Fee, D. W. Tank, and W. Denk, "A miniature head-mounted two-photon microscope: High-resolution brain imaging in freely moving animals," *Neuron* **31**, 903-912 (2001).
11. D. Kim, K. H. Kim, S. Yazdanfar, and P. T. C. So, "Optical biopsy in high-speed handheld miniaturized multifocal multiphoton microscopy," *Proceedings of SPIE* **5700**, 14-22 (2005).
12. D. Bird, and M. Gu, "Fibre-optic two-photon scanning fluorescence microscopy," *J. Microsc.* **208**, 35-48 (2002).
13. L. Giniunas, R. Juskaitis, and S. V. Shatalin, "Scanning Fiberoptic Microscope," *Electron. Lett.* **27**, 724-726 (1991).
14. A. R. Rouse, and A. F. Gmitro, "Multispectral imaging with a confocal microendoscope," *Opt. Lett.* **25**, 1708-1710 (2000).
15. B. Berge, and J. Peseux, "Variable focal lens controlled by an external voltage: An application of electrowetting," *Eur. Phys. J. E* **3**, 159-163 (2000).

16. S. Kuiper, and B. H. W. Hendriks, "Variable-focus liquid lens for miniature cameras," *Appl. Phys. Lett.* **85**, 1128-1130 (2004).
17. A. J. Wright, B. A. Patterson, S. P. Poland, J. M. Girkin, G. M. Gibson, and M. J. Padgett, "Dynamic closed-loop system for focus tracking using a spatial light modulator and a deformable membrane mirror," *Opt. Express* **14**, 222-228 (2006).
18. H. Suchowski, D. Oron, and Y. Silberberg, "Generation of a dark nonlinear focus by spatio-temporal coherent control," *Opt. Commun.* **264**, 482-487 (2006).
19. M. J. Levene, D. A. Dombeck, K. A. Kasichke, R. P. Molloy, and W. W. Webb, "In vivo multiphoton microscopy of deep brain tissue," *J. Neurophysiol.* **91**, 1908-1912 (2004).
20. B. A. Flusberg, J. C. Lung, E. D. Cocker, E. P. Anderson, and M. J. Schnitzer, "In vivo brain imaging using a portable 3.9 gram two-photon fluorescence microendoscope," *Opt. Lett.* **30**, 2272-2274 (2005).
21. Y. Yasuno, S. Makita, T. Yatagai, T. F. Wiesendanger, A. K. Ruprecht, and H. J. Tiziani, "Non-mechanically-axial-scanning confocal microscope using adaptive mirror switching," *Opt. Express* **11**, 54-60 (2003).
22. D. Oron, E. Tal, and Y. Silberberg, "Scanningless depth-resolved microscopy," *Opt. Express* **13**, 1468-1476 (2005).
23. G. H. Zhu, J. van Howe, M. Durst, W. Zipfel, and C. Xu, "Simultaneous spatial and temporal focusing of femtosecond pulses," *Opt. Express* **13**, 2153-2159 (2005).
24. O. E. Martinez, "Grating and prism compressors in the case of finite beam size," *J. Opt. Soc. Am. B* **3**, 929-934 (1986).
25. J. Goodman, *Introduction to Fourier Optics* (Roberts & Company, Englewood, Colorado, 2005).
26. D. G. Ouzounov, K. D. Moll, M. A. Foster, W. R. Zipfel, W. W. Webb, and A. L. Gaeta, "Delivery of nanojoule femtosecond pulses through large-core microstructured fibers," *Opt. Lett.* **27**, 1513-1515 (2002).
27. W. Gobel, A. Nimmerjahn, and F. Helmchen, "Distortion-free delivery of nanojoule femtosecond pulses from a Ti : sapphire laser through a hollow-core photonic crystal fiber," *Opt. Lett.* **29**, 1285-1287 (2004).
28. E. Tal, D. Oron, and Y. Silberberg, "Improved depth resolution in video-rate line-scanning multiphoton microscopy using temporal focusing," *Opt. Lett.* **30**, 1686-1688 (2005).
29. Y. C. Wu, P. Xi, J. N. Y. Qu, T. H. Cheung, and M. Y. Yu, "Depth-resolved fluorescence spectroscopy of normal and dysplastic cervical tissue," *Opt. Express* **13**, 382-388 (2005).
30. M. C. Skala, J. M. Squirrell, K. M. Vrotsos, V. C. Eickhoff, A. Gendron-Fitzpatrick, K. W. Eliceiri, and N. Ramanujam, "Multiphoton microscopy of endogenous fluorescence differentiates normal, precancerous, and cancerous squamous epithelial tissues," *Cancer Res.* **65**, 1180-1186 (2005).
31. W. R. Zipfel, R. M. Williams, R. Christie, A. Y. Nikitin, B. T. Hyman, and W. W. Webb, "Live tissue intrinsic emission microscopy using multiphoton-excited native fluorescence and second harmonic generation," *Proc. National Academy of Sciences of the United States of America* **100**, 7075-7080 (2003).
32. L. Fu, A. Jain, H. K. Xie, C. Cranfield, and M. Gu, "Nonlinear optical endoscopy based on a double-clad photonic crystal fiber and a MEMS mirror," *Opt. Express* **14**, 1027-1032 (2006).
33. A. M. Weiner, D. E. Leaird, J. S. Patel, and J. R. Wullert, "Programmable Femtosecond Pulse Shaping by Use of a Multielement Liquid-Crystal Phase Modulator," *Opt. Lett.* **15**, 326-328 (1990).
34. M. M. Wefers, and K. A. Nelson, "Programmable Phase and Amplitude Femtosecond Pulse Shaping," *Opt. Lett.* **18**, 2032-2034 (1993).

1. Introduction

The advantage of multiphoton microscopy (MPM) for imaging is its ability to perform optical sectioning in highly scattering samples [1]. The application of MPM to a flexible fiber endoscope has been slow due to the difficulty in miniaturizing mechanical scanning components [2]. Transverse scanning has been performed on the proximal end of a fiber bundle in both one-photon confocal [3-5] and two-photon microscopy [6], but focusing and axial scanning invariably requires mechanical motion on the distal end of an endoscope [7, 8]. As seen in recent reports of multiphoton endoscopes [2, 9] and miniature microscopes [10, 11], these mechanical scanning devices are the main limitation in the fabrication of a flexible and compact endoscope, characteristics that are crucial to make multiphoton imaging compatible with existing endoscopes.

A few axial scanning methods have been applied to a two-photon fluorescence (TPF) fiber probe. In the simplest case, axial scanning can be performed by physically moving the sample [12] or a lens at the distal end of the fiber [13]. A hydraulic system has been employed to adjust the suction applied to a tissue specimen, thus changing the focal plane by varying the distance between the fiber and the objective [14] or between the objective and the sample [4]. Also, a liquid lens can be used at the distal end of the fiber, where adjusting the voltage across

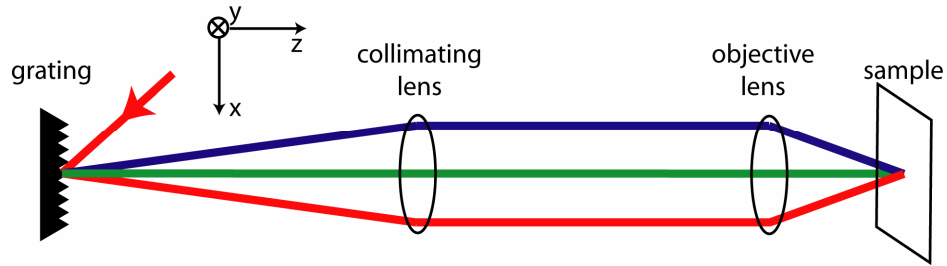


Fig. 1. A typical SSTF setup

the interface of two liquids changes the radius of curvature of the meniscus, thus varying the focal length [15], [16]. A spatial light modulator (SLM) has also been applied to provide wavefront correction and axial focal shift [17, 18]. A disadvantage of these techniques is that they operate at the distal end of the fiber. If the fiber probe is a gradient refractive index (GRIN) lens, however, adjusting the coupling into the proximal end scans the focal plane because the GRIN fiber acts as a thick lens [2, 19]. There are many ways to adjust the coupling into the GRIN lens, including piezo-stages [19], micromotors [20], and an adaptive mirror [21]. However, the rigid nature of the GRIN lens makes it best suited for a rigid endoscope or a miniature microscope. When a GRIN lens is affixed to the end of a flexible fiber endoscope, though, these coupling components must be added to the distal end of the fiber.

Simultaneous spatial and temporal focusing (SSTF), a MPM imaging technique, improves the axial resolution and reduces the background by broadening the pulse width everywhere but at the focal volume [22, 23]. SSTF works by spatially separating the frequencies of a short pulse with a grating, collimating these monochromatic beams with a cylindrical lens, and recombining them with an objective lens (Fig. 1). A temporal focus occurs because the different frequency components only overlap within the focal region of the objective lens. Thus, the pulse width is shortest only at the focal plane, and, as described in [22], the pulse width is transform-limited.

It was mentioned in a previous paper [22] that the presence of group velocity dispersion (GVD) in an SSTF system increases the optical path length of the system. Therefore, the plane of the temporal focus will be displaced along the optical axis from the geometrical focus of the objective lens, yielding z -scanning as a function of dispersion [18]. In this paper, the authors theoretically and experimentally demonstrate that changing the GVD of the system results in axial scanning of the temporal focal plane. In Section 2, we derive the fluorescence signal as a function of dispersion and position z along the optical axis using Fresnel diffraction. In Section 3, we demonstrate experimentally the dependence of focal plane position on GVD, and the remote axial scanning capability in a fiber delivery configuration. In Section 4, we discuss the practical requirements for applying this technique to both a multiphoton microscope and a remote axial scanning, flexible fiber probe.

2. Theoretical analysis of SSTF with GVD

Axial scanning in an SSTF system by tuning the amount of GVD in the beam path can be intuitively understood by following the wavefront of the pulse as it propagates through the system. After diffracting off the grating and being collimated by a lens (Fig. 1), the beam becomes a spread of individual monochromatic beams, creating a one-to-one correspondence between the spectral frequency ω and the transverse position x . Thus, any curvature in the spectral phase will directly translate into a curvature of the wavefront in space. The wavefront is flat for a chirp-free pulse, but if there is any second-order chirp, this quadratic spectral phase will result in a quadratically-curved wavefront. This is equivalent to adding an extra lens in space to the system. Adjusting the amount of GVD is analogous to changing the curvature of the lens, thus shifting the position of the focal plane.

The theoretical understanding of axial scanning with SSTF follows closely the published theory for SSTF [23], except that the incident pulse is now chirped. For one individual frequency ω , the beam amplitude at the input focal plane of the objective lens is:

$$A_1(x, \omega) = A_0 e^{-\frac{\omega^2}{\Omega^2}} e^{-\frac{(x-\alpha\omega)^2}{s^2}} e^{i\beta\omega^2} \quad (1)$$

where A_0 is a normalization constant, $\sqrt{2\ln 2} \cdot \Omega$ is the full-width half maximum (FWHM) of the frequency spectrum of the pulse, $\sqrt{2\ln 2} \cdot s$ is the FWHM of each monochromatic beam in space, α is a constant proportional to the groove density of the grating and the focal length of the collimating lens [24], $\alpha\omega$ is the linear displacement of the monochromatic beam of frequency ω , and 2β is the GVD. The imaginary term in Eq. (1) represents the second-order chirp (quadratic spectral phase) of the input pulse.

In order to analytically describe the field at the output, we follow the paraxial approximation used in Ref. [25] to propagate the beam to the focal volume (for detailed calculations, see the Appendix). The spatially-chirped beam, $A_1(x, \omega)$, is incident upon the input focal plane of the objective lens. First, the Fresnel diffraction formula is applied to A_1 to propagate the beam to the objective lens. After adding the quadratic phase due to the objective lens, the Fresnel diffraction formula is used again to propagate it a distance z toward the focal volume. Fourier transforming back into the time domain expresses the field in the focal volume. To simplify calculations, we assume that the wavevector k for each frequency is approximately k_0 , the wavevector of the center wavelength of the pulse, which is valid for pulse widths on the order of 100 fs. Integrating the squared intensity I over time and the transverse direction x yields the total two-photon excitation (TPE) signal at an axial plane at position z :

$$TPE(z) = \int_{-\infty}^{\infty} \int_{-\infty}^{\infty} I^2(x, z, t) dx dt = \frac{C}{\left[\left(1 + \beta\Omega^2 \frac{z-f}{z_M} \right)^2 + \left(\frac{f-z + \beta\Omega^2 z_R}{z_R} \right)^2 \right]^{\frac{1}{2}}} \quad (2)$$

where $z_M = \frac{2f^2}{k_0 s^2}$, $z_R = \frac{2f^2/k_0}{s^2 + \alpha^2 \Omega^2}$, f is the focal length of the objective lens, C is a constant, and z_M is the Rayleigh length of the focused monochromatic beam. Intuitively, $(s^2 + \alpha^2 \Omega^2)^{\frac{1}{2}}$ is the width of the spatially-chirped beam before the objective lens. Thus, z_R is the Rayleigh length of the focused spatially-chirped beam.

If $\beta\Omega^2$ is small, then Eq. (2) can be approximated as:

$$TPE(z) \approx \frac{C}{\left[1 + \left(\frac{f-z + \beta\Omega^2 z_R}{z_R} \right)^2 \right]^{\frac{1}{2}}} \quad (3)$$

As seen in Eq. (3), the axial response $TPE(z)$ has a peak of constant value C , i.e., independent of GVD, at the temporal focal plane position $z = f + \beta\Omega^2 z_R$. The FWHM of $TPE(z)$ ($2\sqrt{3} \cdot z_R$) defines the axial resolution. Equation (3) also shows that the shift of the focal plane position has a linear dependence on GVD when $\beta\Omega^2$ is small:

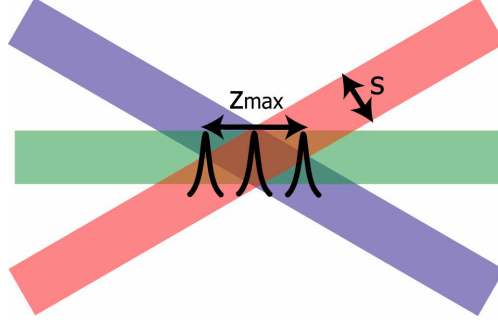


Fig. 2. A ray-tracing representation of the focal volume shows intuitively the fundamental scanning limit, where s is the lateral spot size of a monochromatic beam and Z_{\max} is the length of the geometrical overlap.

$$\Delta z_{\text{shift}} = \beta \Omega^2 z_R. \quad (4)$$

The pulse width at the temporal focus can also be obtained (see the Appendix) as:

$$\tau = \tau_0 \cdot \left[1 + (\beta \Omega^2)^2 \frac{z_R}{z_M} \right]^{\frac{1}{2}}. \quad (5)$$

A small z_R is needed to obtain high axial resolution, but to achieve the desired axial scan range (Δz_{shift}), the dispersion value β must be increased when z_R decreases (Eq. (4)). There will be a limit, however, to the amount of shift that GVD can produce before the assumption that $\beta \Omega^2$ is small is no longer valid. Thus, the exact expression of $TPE(z)$ in Eq. (2) must be used to predict the behavior of $TPE(z)$. In this regime, the maximum value of $TPE(z)$ is no longer a constant and decreases with increasing GVD. Intuitively, the monochromatic beams fail to overlap completely as the temporal focal plane is shifted a large distance away from the geometric focus, therefore broadening the pulse as well as increasing the lateral spot size (Fig. 2). We define the onset of broadening as when the maximum value of $TPE(z)$ in Eq. (2) is reduced to half its value when GVD is zero. Using the approximate peak position as $z = f + \beta \Omega^2 z_R$ and setting Eq. (2) equal to $C/2$, we determine the maximum amount of $\beta \Omega^2$ possible without broadening to be:

$$\beta \Omega^2 \Big|_{\max} = \left(\frac{z_M}{z_R} \right)^{\frac{1}{2}} = \left(\frac{s^2 + \alpha^2 \Omega^2}{s^2} \right)^{\frac{1}{2}} \approx \frac{\alpha \Omega}{s}. \quad (6)$$

Substituting Eq. (6) into our expression for the pulse width (Eq. (5)), the pulse width can be expressed as:

$$\tau = \tau_0 \cdot \left[1 + \left(\frac{\beta \Omega^2}{\beta \Omega^2 \Big|_{\max}} \right)^2 \right]^{\frac{1}{2}}. \quad (7)$$

As seen in Eq. (7), the onset of broadening has been defined as when the pulse width at the temporal focal plane is $\tau = \sqrt{2} \tau_0$. Combining Eq. (4) and Eq. (6), the maximum shift allowed by SSTF is:

$$\Delta z_{\max} = \beta \Omega^2 \Big|_{\max} \cdot z_R = (z_M z_R)^{\frac{1}{2}} \approx \frac{\alpha \Omega}{s} z_R. \quad (8)$$

Equation (8) shows that the number of resolvable z -sections ($\sim \Delta z_{\max} / z_R$) is simply the ratio between the widths of the spatially chirped beam ($\sim \alpha \Omega$) and the monochromatic beam (s) at

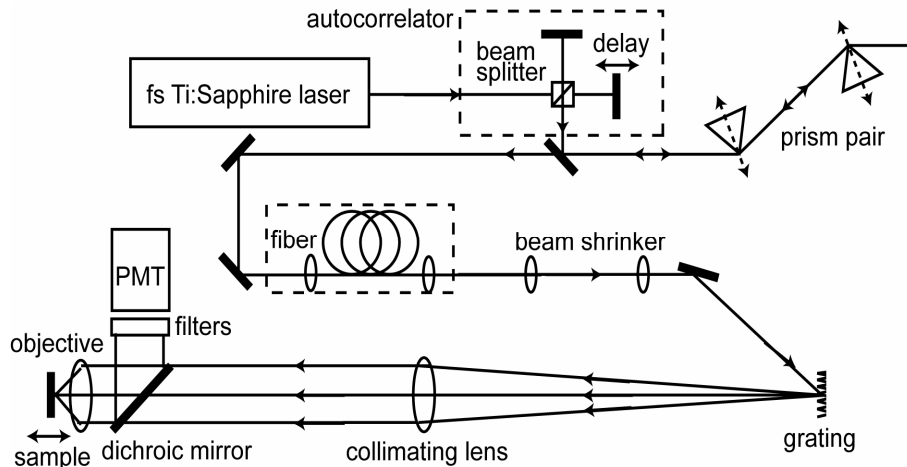


Fig. 3. S STF setup composed of a mode-locked Ti:Sapphire laser tuned to 775 nm, a 1200 lines/mm grating, a 4x beam shrinker, a Zeiss Apochromat 10x/0.45 objective lens, and, for fiber delivery experiments, one meter of large mode area fiber coupled by two 0.1 NA objective lenses.

the input focal plane of the objective lens. In practice, the axial resolution (proportional to z_R) and maximum shift (Δz_{max}) can be scaled for a particular application. For example, a higher z-resolution (smaller z_R) will be possible if the maximum scanning range (Δz_{max}) is sacrificed.

3. Axial scanning experiment

The experimental S STF setup is shown in Fig. 3. We use a mode-locked Ti:Sapphire laser (Spectra-Physics Tsunami) centered at 775 nm with 60-100 fs pulses (assuming a sech shape) at an 80 MHz repetition rate. To measure the pulse width at the sample, the setup has a built-in interferometric second-order autocorrelator which uses TPF from a thin Rhodamine film ($\sim 1 \mu\text{m}$ thick) on a #1 cover glass as the nonlinear element. A prism pair changes the GVD in the system by adjusting the amount of glass in the beam path. A beam shrinker composed of two plano-convex lenses controls the monochromatic beam size s . A ruled diffraction grating with 1200 lines per mm separates the beam into its monochromatic components, which are then collimated by a spherical lens. The objective lens is a 10x/0.45 NA Zeiss Apochromat. To collect the fluorescence signal, a dichroic mirror reflects the TPF signal onto a PMT (Hamamatsu HC125-02) through filters that further remove the excitation light.

In order to observe shifting of the temporal focus, we measure $TPE(z)$ traces by scanning the Rhodamine B film sample on a translation stage. We perform these axial scans at different GVD values and record the peak position, i.e., the position of the temporal focal plane. Figure 4(a) shows the temporal focal plane position as a function of the GVD. A linear relationship is observed between GVD and the displacement of the focal plane, in agreement with theory (Eq. (4)). We are able to shift the temporal focus by more than 130 μm , limited by the thickness of the prisms. Despite the addition of extra dispersion, a nearly transform-limited pulse width is recovered for each of these data points (triangles in Fig. 4(b)). The measured ratio $\alpha\Omega/s$ in our experiment is ~ 22 . For a 65 fs pulse width (bandwidth Ω of 3.8×10^{13} Hz), the recovered pulses are expected to broaden near a GVD value of $3.0 \times 10^4 \text{ fs}^2$ (Eq. (6)), corresponding to a maximum shift of 0.5 mm.

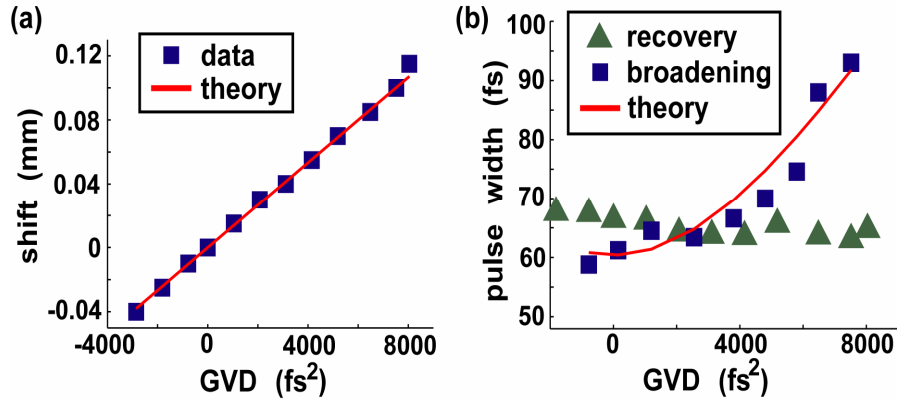


Fig. 4. (a) The shift of the temporal focal plane position is plotted versus GVD varied by adjusting the prism pair. The squares represent peak positions of axial traces taken for various prism positions. The solid line is the expected linear relationship. In (b), the data points represent the pulse width at the sample for various GVD values. The triangles demonstrate the recovery of the pulse width for a 1200 lines per millimeter grating and a 4x beam shrinker. The squares show that the pulse broadens with added GVD when the grating is changed to 600 lines per millimeter and the beam shrinker is reduced to 2x. The solid red line is the predicted pulse width for the broadening case.

In order to demonstrate the broadening of the pulse when the shifting of the focal plane becomes large, we measure the pulse width at the sample using a different set of experimental parameters. Using the same GVD tuning range, we reduce the ratio $\alpha\Omega/s$ to 5 by using a grating with only 600 lines per millimeter, a 2x beam shrinker, and a slightly shorter initial pulse width of 60 fs (Fig. 4(b)). Pulse broadening now occurs at a GVD value of $6.7 \times 10^3 \text{ fs}^2$ yielding a shift of 350 μm . As seen in Fig. 4(b), our experimental results agree reasonably well with the theoretical prediction (Eq. (6) and (7)).

The main advantage of shifting the focal plane by tuning the GVD in SSTF is the ability to perform remote axial scanning in a fiber delivery system, i.e., the scanning mechanism is at the proximal end of the fiber. To demonstrate the feasibility of such a remote axial scanning capability in a fiber delivery system, we insert $\sim 1 \text{ m}$ of large mode area fiber (core diameter 25 μm , Crystal Fibre) between the laser and the grating (Fig. 3). This fiber was chosen due to its low nonlinearity even at high input power [26]. Using a #1 cover glass coated on both sides with a thin film of Rhodamine B, we scan the sample stage through the focal plane at a

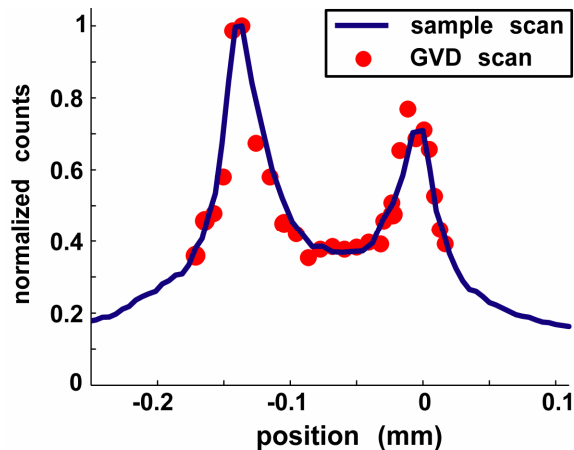


Fig. 5. Scanning of a #1 cover glass coated on both sides with a thin Rhodamine B film. The blue curve is an axial trace obtained by scanning the sample with a translation stage. The red circles represent data taken of the axial scan by tuning the GVD at a fixed sample position.

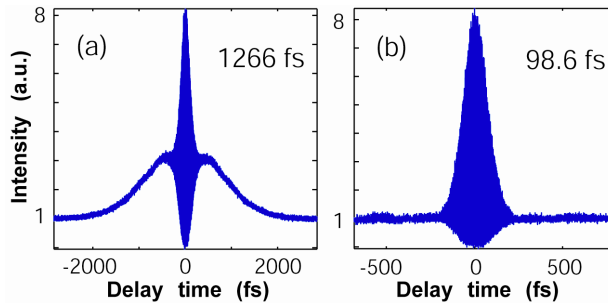


Fig. 6. Autocorrelation traces for a system without dispersion compensation where the pulse has propagated through one meter of large mode area fiber. The laser has a center wavelength of 775 nm and a spectral width of 8 nm. In plot (a), the pulse is at the output of the large mode area fiber, and in (b), at the temporal focal plane of the SSTF setup.

constant GVD value (solid line in Fig. 5). Then, with the sample fixed, we scan through both the front and back films of the slide by adjusting the dispersion in the system (dots in Fig. 5). An extra prism pair is added to the setup in Fig. 5 to increase the GVD tuning range. Thus, we were able to shift the temporal focal plane by 200 microns when z_R is 11.5 microns, revealing both the front and back films of the cover glass. The axial scans obtained by translating the sample and by adjusting the dispersion are nearly identical, demonstrating the feasibility of remote scanning of the focal plane by adjusting the GVD. We note that the z values corresponding to points within the cover glass have been scaled by 1.5 to take into account refraction due to the air-glass interface. The different peak values from the front and back surfaces of the slide are due to a combination of the absorption of the TPF signal of the back film by the front film and the distinct thicknesses of the two films.

In addition, the ability of SSTF to recover a transform-limited pulse width despite the presence of large chirp negates the need for any dispersion pre-compensation in a fiber delivery system (typically by using a prism pair), improving the practicality of the system. For example, when an 87 fs pulse is launched into the large mode area fiber, the pulse broadens to 1.27 ps at the output of the fiber due to its large dispersion (Fig. 6(a)). At the temporal focus, a nearly chirp-free 99 fs pulse width is recovered (Fig. 6(b)) without any dispersion pre-compensation. The 10% pulse broadening is predicted by our theory using the calculated GVD value of the fiber as $3.5 \times 10^4 \text{ fs}^2$. In essence, the SSTF setup acts as a post-dispersion compensation device, automatically removing the chirp of the pulse at the temporal focus. Although fibers have been engineered to exhibit both low nonlinearities and zero dispersion within a specific wavelength range [27], this technique allows short pulses to be delivered to the sample over a broad spectral range without any pre-compensation of dispersion.

4. Discussion

In an SSTF axial scanning setup, the z -resolution (proportional to z_R), lateral spot size (inversely proportional to s), and maximum shift (Δz_{max}) can be scaled for a particular application. For example, a larger lateral spot size (i.e., smaller s) will provide a larger scan range for a given z -resolution. As an example, a 10 micron z -resolution ($z_R=3$ microns) with a spot size of 150 microns can scan 435 microns before the pulse begins to broaden. Alternatively, an improved z -resolution is possible if we sacrifice the maximum scanning range. Tal *et al.* achieved a 1.5 micron z -resolution with temporal focusing for video-rate imaging [28]. For this z -resolution with a 35 micron spot size, the axial scanning range would be 40 microns. Experimentally, the scaling of the z -resolution, lateral spot size, and the maximum scanning range is readily achieved by choosing the right combinations of the focal lengths for the objective and collimating lenses, the groove density of the grating, and the input beam size.

We neglected the vertical dimension in our derivation in Section 2 by assuming the beam

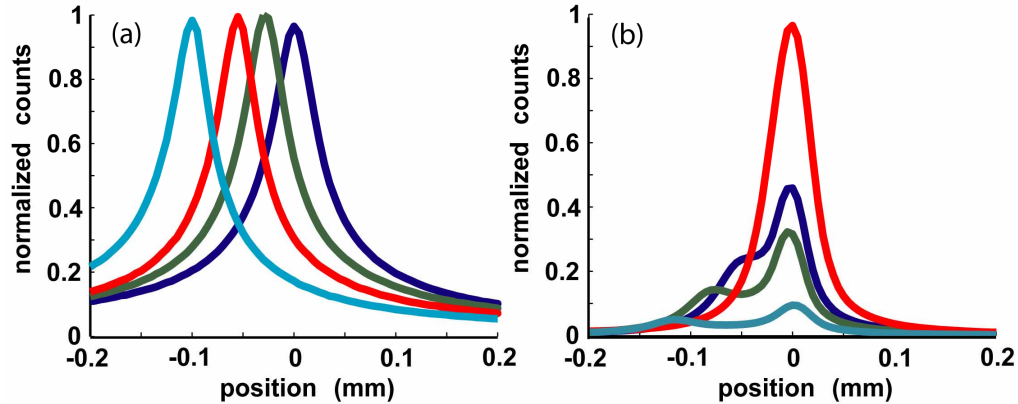


Fig. 7. Axial scan data obtained by GVD tuning for (a) wide-field and (b) line-scanning SSTF.

shape is a thin line in the x -direction at the input focal plane of the objective lens. Here, the width in the x -direction is the spreading of the monochromatic components due to the grating, and the height in the y -direction is the monochromatic beam size s . Because s is small, the y -component of the beam will not focus tightly. Such a focusing configuration is wide-field SSTF because it creates a large spot at the focal plane. In the SSTF line-scanning case, the beam has a circular cross-section at the input focal plane of the objective lens, so that the height (y -dimension) of the monochromatic components will tightly focus to form a line at the geometrical focus. Because TPF is inversely proportional to both the illuminated area and pulse width, the line scanning case results in two peaks when the geometrical and temporal foci do not overlap. To demonstrate this effect experimentally, we expand the y -component of the beam with a cylindrical lens pair. As seen in Fig. 7, changing the dispersion moves the temporal focus, but a stationary peak from the geometrical focus remains. Thus, axial scanning of the temporal focal plane by tuning the GVD works best in the wide-field SSTF configuration.

As opposed to conventional imaging, wide-field imaging with SSTF provides optical sectioning as well as axial scanning using GVD tuning. In practice, the wide-field image is captured on a CCD camera [22]. As the focal plane scans, the camera must be moved back into focus for each temporal focus position. For *in vivo* endoscopic imaging, however, having a moving camera at the distal end of the fiber would be difficult. We believe that the demonstrated remote axial scanning technique is best suited in a passive, flexible fiber probe for multiphoton excitation of z -resolved fluorescence or harmonics, bridging the gap between imaging optical endoscopes and non-imaging fiber optic probes. It has all the desirable attributes of a passive fiber probe but with added z -sectioning capability over an axial scan range of hundreds of microns. As shown previously in tissue spectroscopy and imaging [29-31], the addition of z -sectioning to a conventional fiber probe will undoubtedly improve its capability in medical detection and diagnostics.

To create such a probe, the miniaturization of a typical SSTF setup would need to be considered. First, the fluorescence signal would have to be collected by the delivery fiber. With a large mode area fiber or a double-clad photonic crystal fiber [32], these large cores allow for high collection efficiency throughout the depth of focus as the focal plane is scanned. Second, a dichroic mirror placed at an appropriate angle after the grating can redirect the fluorescence signal into the fiber without affecting the excitation beam. The rest of the optical setup (the collimating lens and the objective lens) is the same as that in an endoscope setup and can be similarly miniaturized.

Fast and electronically-controlled GVD scanning is desirable for remote axial scanning. In our preliminary experiments, translating a pair of prisms into the beam path adjusts the GVD in the system. Although sufficient for demonstrating the concept of remote axial scanning, it is quite slow because linear translation of a bulky prism is necessary. Faster GVD

scanning can be realized based on the same principle except by scanning the optical beam instead of moving the prisms. A regular scan mirror positioned at the focal point of a lens can quickly (up to kHz) redirect the excitation beam so that the amount of glass in the beam path varies, changing the GVD and the chirp of the pulse. In general, axial scanning is done in discrete steps. Thus, an array of varying length glass rods could replace the prisms in order to scan through a range of fixed GVD values. An alternative method would be to manipulate the phase of the beam after the grating using an SLM [33, 34], allowing for fast non-mechanical scanning of the focal plane.

5. Conclusion

We have shown that SSTF allows for shifting the temporal focal plane along the optical axis by adjusting the dispersion in the system. In the limit that GVD is small, the shift of the temporal focal plane is linearly dependent upon dispersion, and the pulse width is transform-limited. When the temporal focus occurs outside of the geometrical overlap of the beams, this relationship breaks down, resulting in a maximum scanning range that is proportional to the axial resolution. We also demonstrated that this method of axial scanning works well for a fiber delivery system, allowing remote axial scanning without any moving parts at the distal end of the fiber. As an added advantage, SSTF automatically compensates for dispersion, allowing fiber delivery systems to recover a transform-limited pulse width at the focus without pre-compensation. We believe a highly promising application of this SSTF technique is an axial-scanning TPF flexible fiber probe with no moving parts at the distal end.

Acknowledgments

This research was made possible by Grant Number 1R21CA115472-01 from the National Cancer Institute (NCI), National Institutes of Health. The authors would like to thank Jesse McMullen for providing the large mode area fiber as well as Kristen Lantz Reichenbach and James van Howe for valuable discussions.

Appendix

The purpose of this appendix is to derive an expression for the intensity I of the field at the focal volume as a function of the axial position z . Using the paraxial approximation, the Fresnel diffraction equation in one dimension [25] is:

$$U_1(x) = \frac{e^{ikf}}{\sqrt{i\lambda f}} \int_{-\infty}^{\infty} U_0(\xi) e^{i\frac{k}{2f}(x-\xi)^2} d\xi. \quad (9)$$

We propagate the field to the objective lens with the Fresnel diffraction equation (Eq. (9)) by substituting $A_1(x, \omega)$ from Eq. (1) into $U_0(x)$ in Eq. (9). The field just before the lens is therefore:

$$\begin{aligned} A_2(x, \omega) &= A_0 \frac{e^{ikf}}{\sqrt{i\lambda f}} e^{-\frac{\omega^2}{\Omega^2}} e^{i\beta\omega^2} \int_{-\infty}^{\infty} e^{-\frac{(\xi-\alpha\omega)^2}{s^2}} e^{i\frac{k}{2f}(x-\xi)^2} d\xi \\ &= A_0 e^{ikf} e^{-\frac{\omega^2}{\Omega^2}} e^{i\beta\omega^2} \frac{1}{\left(1 + i\frac{2f}{ks^2}\right)^{\frac{1}{2}}} e^{-\frac{k(x-\alpha\omega)^2}{2if+ks^2}} \end{aligned} \quad (10)$$

After adding the quadratic phase due to the lens, the field becomes:

$$A_3(x, \omega) = A_0 e^{ikf} e^{-\frac{\omega^2}{\Omega^2}} e^{i\beta\omega^2} \frac{1}{\left(1 + i \frac{2f}{ks^2}\right)^{\frac{1}{2}}} e^{-\frac{k(x-\alpha\omega)^2}{2if+ks^2}} e^{-i\frac{k}{2f}x^2}. \quad (11)$$

By propagating the field a distance z from the lens with the Fresnel diffraction equation (Eq. (9)), the field in the focal volume can be expressed as:

$$A_4(x, z, \omega) = A_0 e^{ik(z+f)} e^{-\frac{\omega^2}{\Omega^2}} e^{i\beta\omega^2} \frac{1}{\left(1 + i \frac{2f}{ks^2}\right)^{\frac{1}{2}}} \frac{1}{\left(1 + i \frac{2z}{ks_1^2}\right)^{\frac{1}{2}}} \dots \frac{(x - \frac{(f-z)\alpha\omega}{f})^2}{s_2^2} e^{-i\frac{k\alpha\omega x}{f}} e^{-i\frac{k\alpha^2\omega^2(z-f)}{2f^2}} \quad (12)$$

$$\text{where } s_1^2 = \frac{4f^2}{k^2 s^2} - i\frac{2f}{k} \text{ and } s_2^2 = \frac{4f^2}{k^2 s^2} + i\frac{2(z-f)}{k}.$$

To simplify calculations, we assume that the wavevector k for each frequency is approximately k_0 , the wavevector of the center wavelength of the pulse. Fourier transforming $A_4(\omega, x, z)$ back into the time domain, the field distribution at the focal volume is:

$$A_5(x, z, t) = \int_{-\infty}^{\infty} A_4(x, z, \omega) \cdot e^{-i\omega t} d\omega = \kappa \cdot e^{-\frac{x^2}{s_2^2}} e^{-\frac{\Omega^2}{4(1+\chi)}(t+\gamma x)^2} \quad (13)$$

where

$$\kappa = A_0 \Omega \sqrt{\frac{i\pi f}{z_M}} \frac{1}{\left[\frac{f-z}{z_M} - 1 + i\left(\frac{f-z}{z_R} + \beta\Omega^2\right)\right]^{\frac{1}{2}}},$$

$$\gamma = \frac{k_0 \alpha / f}{1 + i(z-f)/z_M},$$

$$\chi = \frac{i(z-f)/z_B - i\beta\Omega^2}{1 + i(z-f)/z_M},$$

$$z_M = \frac{2f^2}{k_0 s^2}, z_R = \frac{2f^2/k_0}{s^2 + \alpha^2 \Omega^2}, \text{ and } z_B = \frac{2f^2}{k_0 \alpha^2 \Omega^2}.$$

The intensity can then be expressed as:

$$I(x, z, t) = |A_5|^2 = \left| \kappa e^{-\frac{x^2}{s_2^2}} e^{-\frac{\Omega^2}{4(1+\chi)}(t+\gamma x)^2} \right|^2. \quad (14)$$

The pulse width at the temporal focus can be obtained by substituting $z = f + \beta\Omega^2 z_R$ and $x=0$ into Eq. (14). The pulse width τ at the temporal focus is:

$$\tau = \tau_0 \left[1 + (\beta\Omega^2)^2 \frac{z_R}{z_M} \right]^{\frac{1}{2}} \quad (15)$$

where $\tau_0 = \frac{\sqrt{2}}{\Omega}$ is the transform-limited pulse width. At the maximum shift defined by Eq. (6), the pulse width broadens to $\tau = \sqrt{2}\tau_0$. Similarly, the lateral spot size at the temporal focus can be calculated by substituting $z = f + \beta\Omega^2 z_R$ and $t=0$ into Eq. (14). This yields the lateral spot size at the temporal focus:

$$s_3 = s_3^{(0)} \left[1 + (\beta\Omega^2)^2 \frac{z_R}{z_M} \right]^{\frac{1}{2}} \quad (16)$$

where $s_3^{(0)}$ is the lateral spot size when GVD is zero. Therefore, at the onset of broadening (Eq. (6)), the lateral spot size stretches to $s_3 = \sqrt{2}s_3^{(0)}$.